Fatigue crack growth in Haynes 230 single crystals: an analysis with digital image correlation

S. RABBOLINI[1], G. J. PATAKY[2], H. SEHITOGLU[2] and S. BERETTA[1]

[1]*Department of Mechanical Engineering, Politecnico di Milano, Via La Masa 1, 20156, Milan, Italy,* [2]*Department of Mechanical Science and Engineering, University of Illinois at Urbana-Champaign, 1206 W Green Street, 61801, Urbana, IL USA*

ABSTRACT   Fatigue crack growth was investigated in Haynes 230, a nickel-based superalloy. Anisotropic stress intensity factors were calculated with a least squares algorithm using the displacements obtained from digital image correlation. Crack opening/sliding levels were measured by analysing the relative displacement of crack flanks. Reversed crack tip plastic zones were calculated adopting an anisotropic yield criterion. The strains measured in the reversed plastic zone by digital image correlation showed a dependence on crystallographic orientation. Finally, a finite element model was adopted to examine plasticity around the crack tip. Results were compared with the experimentally observed strains.

Keywords   effective stress intensity factor range; fatigue crack growth; mixed-mode propagation; plastic zone; single crystal nickel-based alloy; single crystal plasticity.

NOMENCLATURE

a_{ij} = Elastic constants
A = Rigid body rotation
B_u = Horizontal rigid body translation
B_v = Vertical rigid body translation
C = Paris law coefficient
g = Slip system strength
h_0 = Slip system initial hardening modulus
$h_{a\beta}$ = Single crystal hardening matrix
K_I = Mode I stress intensity factor
K_{II} = Mode II stress intensity factor
n = Paris law exponent
q = Latent hardening coefficient
r = Radial distance from crack tip
R = Load ratio
S = Yield stress in the shear direction (Hill's criterion)
t = ratio between ΔK_{II} and ΔK_I
T = T-stress term
u = Horizontal displacements
v = Vertical displacements
X, Y, Z = Yield stress in the principal directions (Hill's criterion)
z = Rate sensitivity exponent
α = Energy release rate ratio factor
γ = Shear strain
ΔK_I = Mode I stress intensity factor range
ΔK_{II} = Mode II stress intensity factor range
$\Delta K_{I,eff}$ = Mode I effective stress intensity factor range
$\Delta K_{II,eff}$ = Mode II effective stress intensity factor range
ΔK_{tot} = Combined stress intensity factor range

Correspondence: S. Rabbolini. E-mail: silvio.rabbolini@polimi.it

$$\Delta r_p = \text{Reversed plastic zone radius}$$
$$\sigma_x, \sigma_y = \text{Stress in the } x \text{ and } y \text{ direction respectively}$$
$$\tau_{xy} = \text{Shear stress in the } x\text{--}y \text{ plane}$$
$$\tau_s = \text{Resolved stress on the slip system}$$
$$\tau_0 = \text{Critical resolved shear stress}$$
$$\Im_i = \text{Mode i energy release rate}$$
$$\vartheta = \text{The angular coordinate from the crack tip}$$

INTRODUCTION

The continuous research for sustainable and efficient energy has led to the renewed interest in nickel-based alloys in the power generation industry. In particular, nickel-based superalloys exhibit good resistance to creep and corrosion, properties that make them the preferable choice for components working in aggressive conditions. A further enhancement in material's properties can be obtained by changing not only the alloying elements but also the crystal structure. In order to increase creep properties, single crystals are the most adopted structure for components such as turbine blades, because such a structure does not include polycrystalline grain boundaries. Grain boundaries are the location in which voids, responsible for creep failure, originate and grow. On the other hand, the adoption of single crystal components requires an accurate design, because single crystals exhibit a marked anisotropic behaviour and crack propagation occurs along directions related to the crystal slip plane orientations.[1] In this paper, fatigue crack growth in single crystals of a commercially available nickel-based superalloy, Haynes 230, is investigated at room temperature in order to remove environmental effects, such as oxidation. The main focus of this research is to accurately analyse fatigue crack growth in order to implement Haynes 230 single crystals into a damage-tolerant design.

Fatigue crack growth has been investigated intensively in the past few decades. Initial works analysed crack propagation in polycrystals and mainly dealt with tensile opening, also known as Mode I. Paris and Erdogan[2] correlated crack growth rates, *da/dN*, with Mode I stress intensity factor ranges, ΔK_I, through the Paris relationship. An intensive study of the early crack propagation phase in nickel-based superalloy single crystals[3] showed that a crack in a crystal usually propagates along a {111} slip plane. This means that single crystal orientation determines the crack propagation plane, which is not necessarily perpendicular to the opening load. These observations introduced the necessity to study crack propagation in presence of sliding, also referred as Mode II, and its interaction with Mode I growth. Works dealing with mixed-mode propagation[4] showed that crack growth rates under these loading conditions are a function of both ΔK_I and ΔK_{II}. In this work, an accurate analysis of mixed-mode propagation is presented. Mode I and Mode II

stress intensity factor ranges were extracted from the displacements experimentally measured around the crack tip.

A crack tip represents a singularity point in the stress, strain and displacement fields. An analytical description of the stress field around a crack tip in an elastic and isotropic body was given by Williams[5] with an infinite power series. Williams discovered that the singularity around the crack tip is of the order $r^{-1/2}$, where r is the radial distance from the crack tip, and that stress intensity factors are a measure of the singularity itself. Taking into account the effects of anisotropy, Sih *et al.*[6] showed that the singularities introduced by a defect in an anisotropic body are of the same order. In this work, the analytical solution provided by Sih was fitted with the experimental displacements measured by digital image correlation (DIC).

Digital image correlation was originally employed in fatigue crack growth analysis to measure the effects of crack closure.[7,8] Crack tip opening loads were locally measured with two points digital extensometers, following Elber's proposal.[9,10] The idea to extract stress intensity factors from DIC was originally proposed by McNeill *et al.*[11] Carroll *et al.*[12] introduced the necessity to include the second term of William's stress expansion, the *T*-stress, in the *K*-extraction algorithm, whereas Yoneyama *et al.*[13] extracted both ΔK_I and ΔK_{II} during mixed-mode propagation. Recently, DIC was successfully applied to analyse fatigue crack growth in 316 L steel single crystals[14] and to study crack propagation both at room and at high temperature in Haynes 230 polycrystals.[15] An important aspect of these techniques was that, because they were applied on experimental displacements, they included plasticity induced crack closure, allowing for the determination of the effective stress intensity factor range (ΔK_{eff}).

Digital image correlation also provides a means to measure the strain field around the crack tip. The presence of the singularity is responsible for the local yielding and for the high plastic strains present around the crack tip. An estimation of the extent of the plastic zone can also be obtained using the stress intensity factor ranges measured by regression with a yield criterion. A Mode I loaded crack in an isotropic body exhibits a symmetric plastic zone, whereas in the case of mixed-mode loading (I + II), the plastic zone shape has been described as asymmetric.[16,17] Because of their orientation with respect to the loading axis, inclined cracks can experience mixed-mode loading; the angle of this

inclination has shown to have an effect on the plastic zone shape.[18,19] Gao et al.[20] observed that the T-stress term becomes significant on plastic zone size only at moderate stress levels, whereas Betegon and Hancock[21] demonstrated that T-stress can change plastic zone size. Inside this plastic zone, a smaller area experiences reversed plastic flow during each load cycle. Rice estimated that the extension of this zone is one quarter of the monotonic plastic zone,[22] whereas McClung and Sehitoglu[23] demonstrated that its extension depends on the amount of crack closure.

A more accurate description of the crack tip plastic zone can be obtained using crystal plasticity models. Crystal plasticity model formulation is mainly due to the works of Taylor, Rice, Hill, Asaro and Needleman.[24–27] In these models, inelastic strain in crystals is related to slip occurring in particular crystallographic planes. Rice[28] applied single crystal plasticity to a model containing a crack and calculated the extension of the yielded zone around the crack tip. Since then, several works have been published about the numerical analysis of crack tip in single crystal. In particular, Flouriot et al.[29] analysed the effects of the thickness in the plastic zone extension from a single crystal C(T) specimen, whereas Potirniche et al.[30] compared analytical plastic zone radii with those obtained from numerical single crystal simulations. All these analyses were carried out considering monotonic loads. Gall et al.[31] applied single crystal plasticity to fatigue crack growth and measured crack opening loads, while Potirniche et al.[32] applied the same concepts to short crack propagation in aluminium.

This study deals with mixed-mode crack propagation in Haynes 230 single crystals, which is important for understanding crack propagation mechanisms in individual grains. Crack propagation driving forces were measured using the displacement field around the crack tip during fatigue cycles. Opening and sliding levels were measured from crack flanks displacements obtained from virtual extensometers. The first part of this paper discusses material properties, the experimental setup and the procedure for testing. The analysis section presents a brief description of the regression algorithm with a discussion of the plastic zone evaluation. In the results section, fatigue crack growth results are discussed in terms of crack opening levels, crack growth rates and plastic zone shapes and sizes. Finally, the results obtained from finite element models simulating single crystal plasticity are compared with those experimentally measured.

EXPERIMENTS

Material and fatigue testing

Commercially available Haynes 230 was used for testing. Haynes 230 is a nickel-based superalloy, which exhibits good corrosion and creep resistance because of the addition of chromium, molybdenum and tungsten. The Haynes 230 chemical composition is provided in Table 1.

Single crystals were obtained from a seed, adopting the Bridgman technique in vacuum: its initial orientation was determined using electron backscatter diffraction; at this point, slices parallel to $\{1\bar{1}0\}$ plane were cut. The choice of this plane is due to the fact that it contains both of the crystallographic orientations of interest, that is, [001] and [111].

Single-edge notch tension specimens were employed for the experimental campaign. Notches were made by electrical discharge machining. The specimen's width, gauge length and notch depth were 3.0, 8.0 and 0.5 mm respectively; the [111] oriented specimen thickness was 1.3 mm, whereas the [001] oriented crystal was 1.09 mm thick. A schematic of the specimen geometry is shown in Fig. 1. Tensile properties of the two orientations of interest, obtained from monotonic tests on unnotched specimens, are shown in Table 2.

Before testing, specimens were prepared by mechanically polishing the surface to a mirror finish with abrasive paper, up to a grit of P2400. A speckle pattern, necessary for DIC, was then applied onto each specimen using black paint. In order to obtain a refined speckle pattern, necessary for high-quality measurements, an airbrush with a 0.18 mm wide nozzle was employed for painting. Images were acquired by a digital camera, whose resolution and maximum frame rate were, respectively, 1600 by 1200 pixel and 15 fps. A magnification of 2.7×, obtained using an adjustable lens with a 12× magnification range and a 2× adapter was employed during the tests. This setup allowed a resolution of 0.63 μm/pix. The experimental setup is shown in Fig. 1. Tests were performed with a cyclic

Table 1 Chemical composition (wt%) of Haynes 230

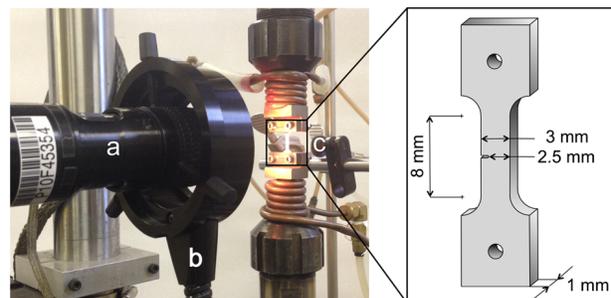| Al	B	C	Co	Cr	Cu	Fe	La	Mn
0.35	0.005	0.1	0.16	22.14	0.04	1.14	0.015	0.5
Mo	Ni	P	S	Si	Ti	W	Zr	–
1.25	bal	0.005	0.002	0.49	0.01	14.25	0.01	–

Fig. 1 The experimental setup and a schematic of specimen geometry: (a) camera and lens, (b) light source and (c) specimen.

Table 2 Selected tensile properties of Haynes 230 alloy specimens

Crystallographic orientation	Yield stress, 0.2% offset (MPa)	Elastic modulus (GPa)
[001]	274	137
[111]	428	330

frequency of 5 Hz on a servo-hydraulic load frame with a fixed load ratio R equal to 0.05. [111] oriented specimen was subjected to a cyclic load with a stress range of 181 MPa. The stress range was reduced to 133 MPa for the [001] crystal, because this orientation exhibited lower yield stress.

Image acquisition and the servo-hydraulic load frame were controlled by a computer, which registered images and their respective applied loads, measured by a 7.5 kN load cell. After crack initiation, measurement cycles were run periodically at a rate of 0.25 Hz to obtain a greater number of images per cycle, providing the possibility of a more accurate fatigue cycle analysis.

After the end of the fatigue test, electron backscatter diffraction was performed on the specimens in order to verify their orientations. For the [001] specimen, the normal was determined to be $[4\bar{3}0]$, and the transverse direction was [340]. The [111] specimen had a normal direction of $[0\bar{1}1]$, and thus, the transverse orientation was $[2\bar{1}\bar{1}]$. A schematic of the two specimens indicating the loading directions in the crystal frame is shown in Fig. 2. (111) slip planes are shown in cyan, whereas crack propagation planes are represented in purple.

Digital image correlation procedure

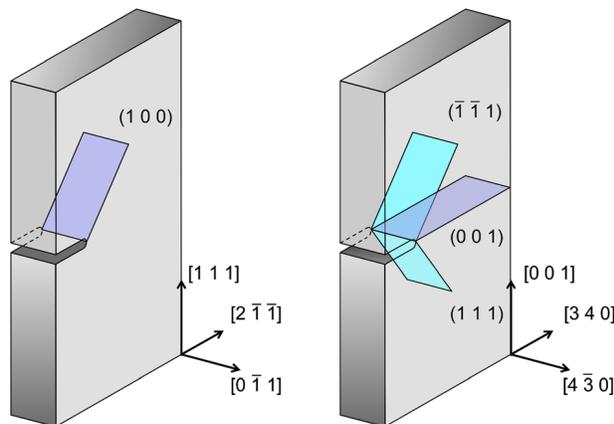The experimental displacements measured by DIC are the starting point for the analysis presented in this paper.

Fig. 2 A schematic of the samples in the crystal frame showing the loading directions, [111] slip planes in cyan and crack propagation planes in purple.

DIC compares the differences in the speckle pattern light intensity between reference and deformed images to determine the displacements. Square groups of pixels, called subsets, are tracked in order to obtain the best correlation between the two images.

Digital image correlation analysis was performed using a commercially available image correlation software (Vic-2D produced by Correlated Solutions, Columbia, SC, USA). The first picture of each measurement cycle, taken at the minimum applied stress, was used as the reference image for that cycle. Full field images were correlated to get horizontal and vertical displacements. This means that during calculations, points before and beyond crack tip were considered. Displacements were calculated using square subsets, whose maximum dimensions were 51 by 51 pixels. These displacements were then employed to evaluate stress intensity factor ranges (ΔK) following the procedure discussed in Section 4.

Two-point virtual extensometers were employed to measure the crack opening/sliding loads. This feature tracks two subsets, one on each side of the crack flanks, as shown in Fig. 3a. Several virtual extensometers were applied on the length of the crack flanks, in order to get an accurate displacement profile during cyclic loading. In order to get the pure vertical (ΔU_I) and horizontal (ΔU_{II}) displacements, virtual extensometers were placed perpendicular to the crack flanks. Once rotated to the crack coordinate system (Fig. 3c), the difference in the vertical crack tip displacements, $\Delta v = v_{upper} - v_{lower}$, was employed to describe Mode I opening, whereas the horizontal crack tip displacements, $\Delta u = u_{upper} - u_{lower}$, were used to describe Mode II crack sliding.

Effective stress intensity factor ranges extraction

The adoption of DIC allows for the determination of a full displacement field, which can be used to evaluate crack propagation driving forces without geometric considerations. A nonlinear least-squares regression can be used to determine effective stress intensity factor ranges and how they change during a load cycle. The procedure described by Pataky *et al.*[14] is adopted.

During the measurement cycles, the cyclic frequency was slowed down and the entire loading and unloading parts of the cycle were recorded. These displacements were the starting points for the ΔK_I, ΔK_{II} and T-stress calculations. For a mixed-mode loaded crack, the crack tip displacements for an orthotropic material are described by Eqs (1) and (2), as previous work.[6,33] In this set of equations, horizontal and vertical displacements, together with material elastic constants, are referred to the local crack tip coordinate system, as shown in Fig. 3c.
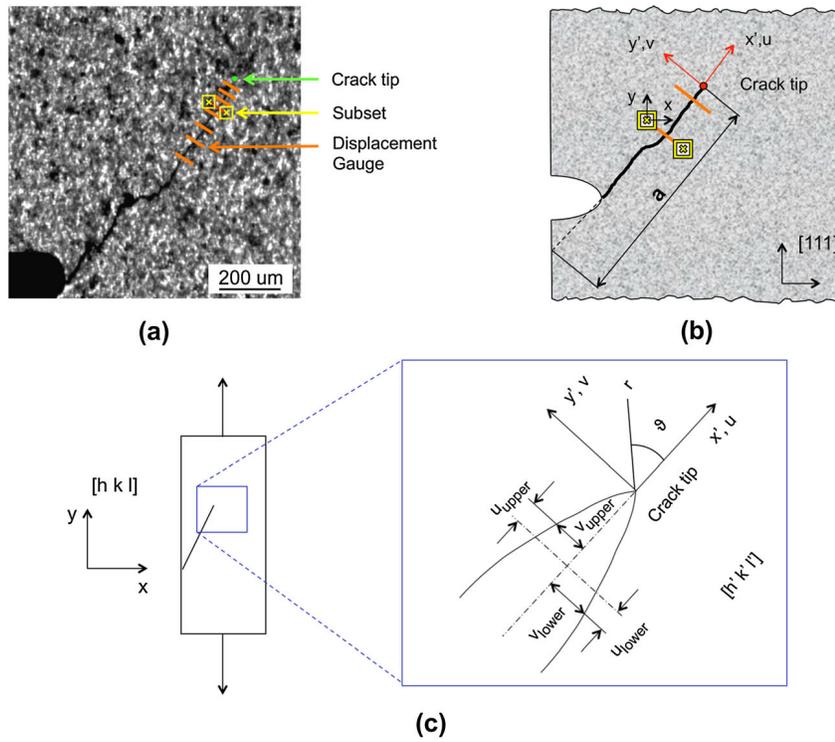
(a)

(b)

(c)

Fig. 3 (a) An example of virtual-extensometers disposition on the [111] specimen. (b) A schematic showing the displacements measured by extensometers. (c) Coordinate system for measuring crack opening and sliding displacements and for extracting ΔK_{eff}.

$$u = K_I\sqrt{\frac{2r}{\pi}}\text{Re}\left\{\frac{1}{\mu_1-\mu_2}\left[\mu_1 p_2\sqrt{\cos\vartheta+\mu_2\sin\vartheta}-\mu_2 p_1\sqrt{\cos\vartheta+\mu_1\sin\vartheta}\right]\right\}+K_{II}\sqrt{\frac{2r}{\pi}}\times$$
$$\text{Re}\left\{\frac{1}{\mu_1-\mu_2}\left[p_2\sqrt{\cos\vartheta+\mu_2\sin\vartheta}-p_1\sqrt{\cos\vartheta+\mu_1\sin\vartheta}\right]\right\}+a_{11}Tr\cos\vartheta-Ar\sin\vartheta+B_u \quad (1)$$

$$v = K_I\sqrt{\frac{2r}{\pi}}\text{Re}\left\{\frac{1}{\mu_1-\mu_2}\left[\mu_1 q_2\sqrt{\cos\vartheta+\mu_2\sin\vartheta}-\mu_2 q_1\sqrt{\cos\vartheta+\mu_1\sin\vartheta}\right]\right\}+K_{II}\sqrt{\frac{2r}{\pi}}\times$$
$$\text{Re}\left\{\frac{1}{\mu_1-\mu_2}\left[q_2\sqrt{\cos\vartheta+\mu_2\sin\vartheta}-q_1\sqrt{\cos\vartheta+\mu_1\sin\vartheta}\right]\right\}+a_{12}Tr\sin\vartheta+Ar\cos\vartheta+B_v \quad (2)$$

where Re stands for the real part of a complex number, and

$$p_i = a_{11}\mu_i^2 + a_{12} - a_{16}\mu_i \quad (3)$$

$$q_i = a_{12}\mu_i + \frac{a_{22}}{\mu_i} - a_{26} \quad (4)$$

K_I and K_{II} are the Mode I and Mode II stress intensity factors, T is the T-stress, A is the rigid body rotation, B_u

and B_v are rigid body translations in the horizontal and vertical directions, r and ϑ are the polar coordinates considering the origin at the crack tip and a_{ij} are the elastic constants of nickel, as reported by Hertzberg.[34] μ_1 and μ_2 are the two complex conjugate roots from the Eq. (5) for which the imaginary parts are positive.

$$a_{11}\mu^4 - 2a_{16}\mu^3 + (2a_{12}+a_{66})\mu^2 - 2a_{26}\mu + a_{22} = 0 \quad (5)$$

In Eq. (2), the vertical displacements responsible for Mode I opening are perpendicular to the crack surface. Because of this, both the horizontal and vertical displacements obtained from DIC and the compliance tensor were rotated with respect to the crack propagation angle. An algorithm was written to solve every displacement using Eqs (1) and (2) to obtain the desired parameters ($K_I, K_{II}, T, A, B_u, B_v$), using a nonlinear least square regression. The last two terms of Eqs (1) and (2) were employed to remove rigid motion and rotation from the K evaluation.

This approach, based on experimentally measured displacements and continuum mechanics, provides a tool, which is useful to correlate crack growth rates to crack propagation driving forces. It should be remarked, however, that an accurate analysis of crack propagation in single crystals requires the description of crystals deformation mechanisms, such as slip. Because of this, a numerical model, which considered single crystal plasticity, is discussed in Section 4, in order to check the validity of the proposed method.

RESULTS

Crack closure measurements

Horizontal and vertical displacements were recorded for each virtual extensometer during the fatigue cycle. Because no Mode II sliding was observed in the [001] specimen, only vertical displacements around the crack tip were observed. The measured vertical displacements for a crack size of 1.23 mm are provided in Fig. 4a. The crack starts opening at 10% of the maximum applied load, starting from the notch. At this point, the crack tip still stays closed. The crack tip opening is evident only at 19.8% of the maximum applied stress.

The crack opening displacement profiles for the [111] single crystal specimen are shown in Fig. 5a and b. In this case, both vertical and horizontal displacements are expected, because the crack grows at an angle. In Fig. 5a, vertical displacements are displayed: the crack starts opening from the notch at nearly 20% of the maximum load, but crack tip opening becomes evident only at 39.6%. Mode II displacement profiles are depicted in Fig. 5b: the crack starts opening at 10% of the maximum applied load, starting from the notch. At this point, the crack tip is still closed. The crack tip starts opening at 19.8% of the applied load, whereas it appears fully open at 26.4% of the maximum applied stress.

Using the crack opening displacement profiles, the crack closure phenomena in both Mode I and Mode II were measured and summarised in Fig. 4b for the [001] oriented crystal, whereas the results of the [111] oriented specimen are reported in Fig. 5c. The study of horizontal and vertical displacements allows for the quantification of the crack opening and sliding. The results of both the specimens tested shows that cracks were closed for approximately 20% of the loading cycle. Because in the [001] oriented crystal, the crack propagated perpendicular to the loading axis, only pure Mode I was observed, as shown in Fig. 4b: crack opening level was constant during the propagation and was about 20% of the maximum applied load. The testing on the [111] oriented crystal allowed the study of mixed-mode propagation, because the crack grew at an angle. As depicted in Fig. 5c, the crack exhibited a Mode I opening at about 40% of the maximum applied loading, whereas Mode II sliding was observed at approximately 20%.

Stress intensity factor ranges and Paris curve calculations

The regression analysis calculates all the variables necessary to fit the displacements around the crack tip during a fatigue crack growth cycle, using Eqs (1) and (2). These displacements will be referred to as the regressed
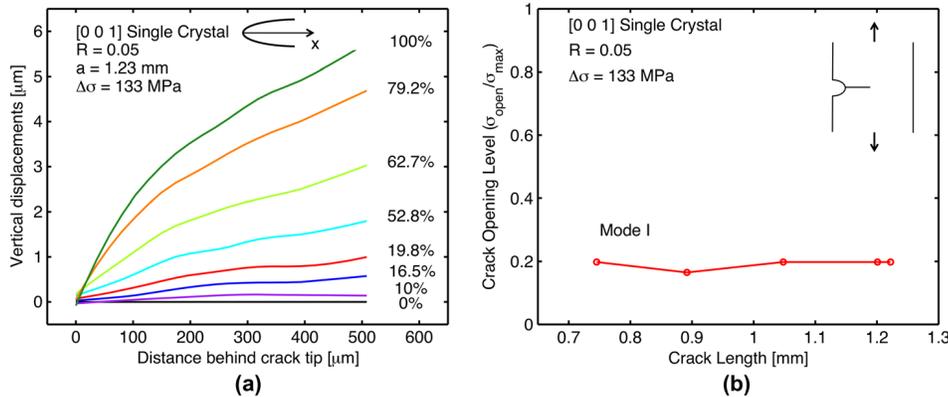

Fig. 4 Virtual extensometers for the [001] oriented specimen. (a) The vertical crack opening displacement profiles of the [001] single crystal specimen at $R = 0.05$ and $\Delta\sigma = 133$ MPa with a measured crack length of 1.23 mm. (b) Crack opening levels for the [001] oriented crystal.
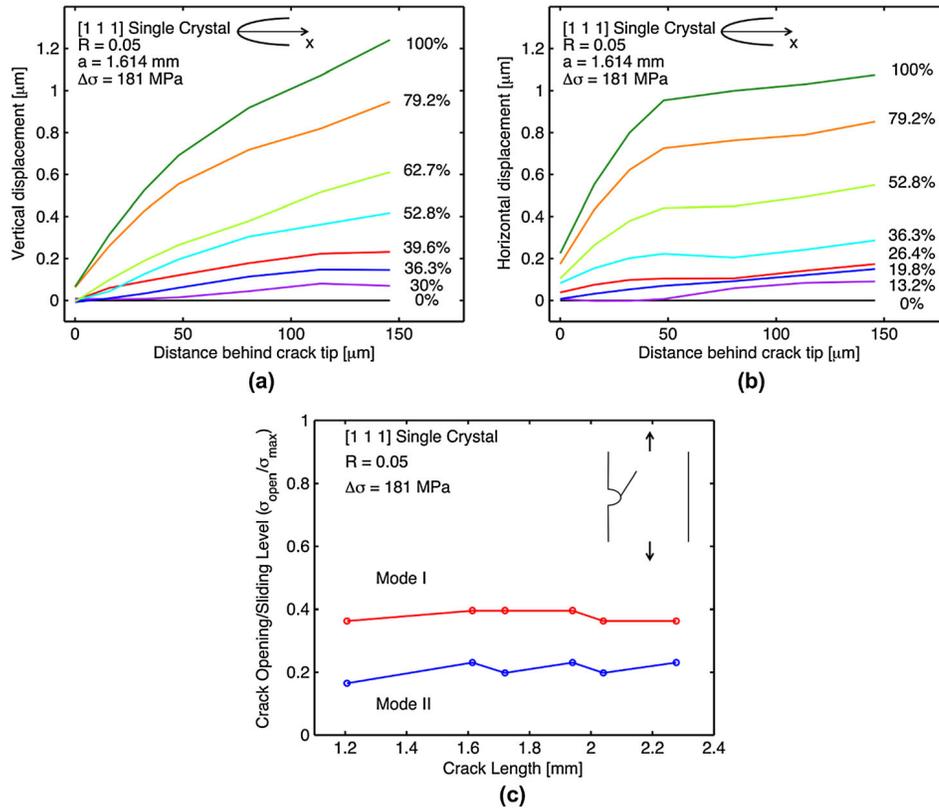
Fig. 5 Virtual extensometers for the [111] oriented specimen. (a) The vertical crack opening displacement profiles of the [111] single crystal specimen at $R = 0.05$ and $\Delta\sigma = 181$ MPa with a 1.614 mm long crack. (b) The horizontal crack sliding displacement profiles of the [111] single crystal specimen at $R = 0.05$ and $\Delta\sigma = 181$ MPa with a 1.614 mm long crack. (c) Crack opening/sliding levels for the [001] oriented crystal.

displacements. The experimentally obtained displacements have been compared with those calculated by regression to show technique accuracy. In Figs 6 and 7, the blue contours represent the displacements experimentally measured, whereas the regression displacements are represented by red lines. The crack tip position is described by a black mark and crack profile is represented by a solid black line. Crack tip position was chosen in order to minimise the mean square error between regressed and experimental displacements, because the presence of the speckle pattern
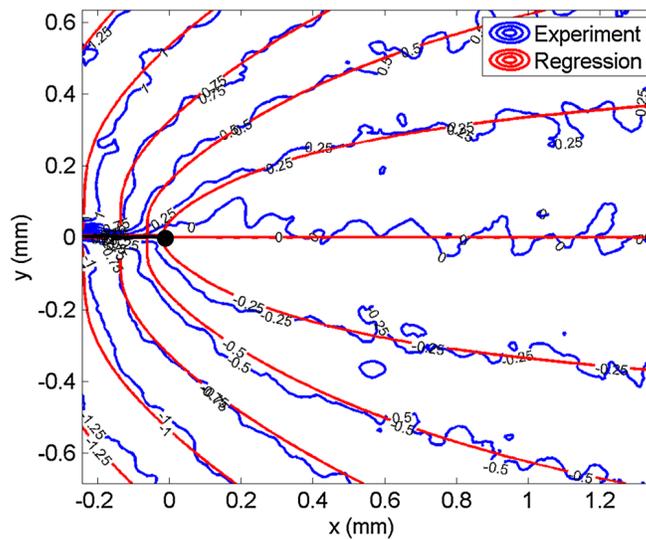

Fig. 6 Comparison of experimentally measured and regression vertical displacement contours in micrometres for the [001] oriented single crystal. The crack length is 0.775 mm with a corresponding ΔK_I regression value of 10.78 MPa$\sqrt{\text{m}}$.
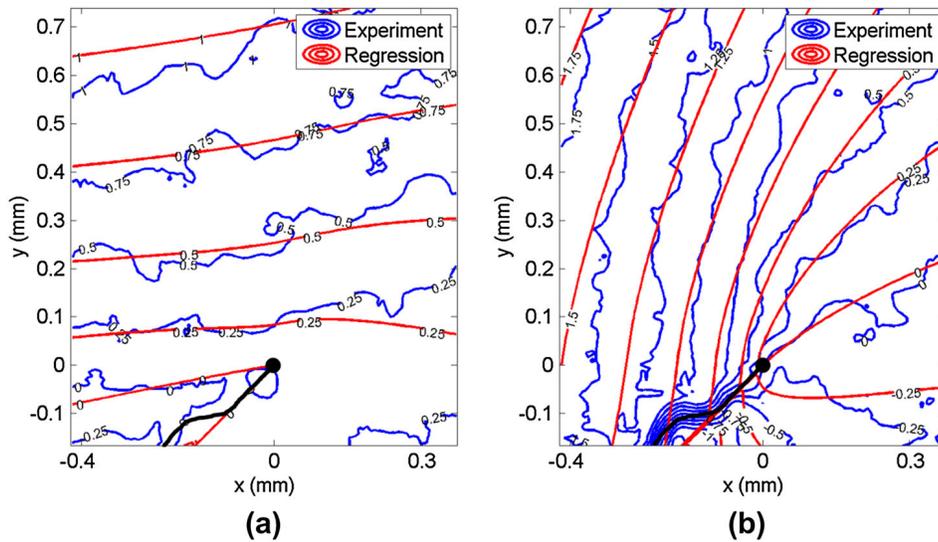
Fig. 7 Comparison of experimentally measured and regression (a) horizontal and (b) vertical displacement contours for the [111] oriented single crystal. The crack is 1.46 mm long with corresponding regression values for ΔK_I of 9.3 MPa$\sqrt{m}$ and ΔK_{II} of 9.4 MPa$\sqrt{m}$.

made it difficult to find the exact tip location. This procedure does not invalidate the accuracy of stress intensity factor ranges measurements, because a few pixels error in positioning implies an error in crack tip estimation of only few microns. For each sample tested, a selected fatigue cycle is shown at the maximum applied load.

When the regression was applied on the [001] specimen, the Mode II stress intensity factor was nearly zero, mainly because of the absence of the shear component, due to the fact that the crack grew in a plane perpendicular to the applied load direction. In Fig. 6, the vertical displacements for the [001] oriented specimen are depicted, showing good agreement between theory and experiments.

The specimen with the [111] orientation was employed for the mixed-mode propagation study: in Fig. 7a and b, vertical and horizontal experimental displacements are compared with those provided by regression. The asymmetry in the horizontal displacement field underlines the presence of Mode II sliding. As in the previous case, the displacement fields obtained from regression are in good agreement with those experimentally measured.

The most general expression for combining ΔK_I and ΔK_{II} has the form[4]:

$$\Delta K_{tot} = \sqrt{(\Delta K_I)^2 + \alpha(\Delta K_{II})^2} \quad (6)$$

where α is the ratio of the energy release rates, $\Im_i$, for Mode II and Mode I, respectively, calculated as proposed in Eqs (7) and (8).[6] In this study, the values of α varied from 1.11 to 2.06.

$$\Im_1 = \frac{\pi \Delta K_I}{2} a_{22} \text{Im} \left[\frac{\Delta K_I(\mu_1 + \mu_2) + \Delta K_{II}}{\mu_1 \mu_2} \right] \quad (7)$$

$$\Im_{II} = \frac{\pi \Delta K_{II}}{2} a_{11} \text{Im}[\Delta K_{II}(\mu_1 + \mu_2) + \Delta K_I \mu_1 \mu_2] \quad (8)$$

Because the majority of the propagation occurred in the steady state region of crack growth, also known as region II propagation, the experimental data were fit to the Paris law, Eq. (9), and the constants C and n are given in Table 3.

$$\frac{da}{dN} = C \left[(\Delta K_{I,eff})^2 + \alpha (\Delta K_{II,eff})^2 \right]^{n/2} \quad (9)$$

In Fig. 8, experimental points obtained from regression for the two experiments performed are compared with the results obtained from polycrystal testing, provided by Pataky *et al.*[15] Despite the different crystallographies, the material shows a common trend, demonstrating the importance of crack-closure in crack propagation. Haynes 230 shows a good fatigue crack growth resistance, compared with other Ni-based superalloys, such as Inconel 718, which exhibits a higher exponential coefficient ($n \approx 4$).[35] The data-fitting coefficients proposed in Table 3 are in agreement with those reported in literature[15,36] and demonstrate that fatigue crack growth in Haynes 230 at

Table 3 Effective Paris law fits and stress intensity threshold from fatigue crack growth tests of Haynes 230 alloy

Specimen	C	n
[111] single crystal	1.79×10^{-9}	2.91
[001] single crystal	8.04×10^{-10}	3.48
Data-fitting	1.55×10^{-9}	2.96

Crack growth rates measured in mm/cycle and stress intensity factor ranges in $MPa\sqrt{m}$.
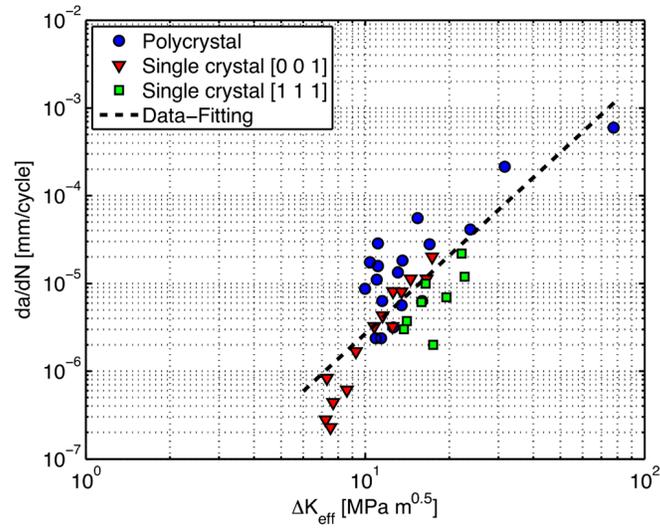
Fig. 8 Fatigue crack growth results for the polycrystalline and single crystal Haynes 230 specimens at room temperature.

room temperature is similar to crack propagation in a traditional steel ($n \approx 3$).

STRAIN IRREVERSIBILITY AT THE CRACK TIP

Cyclic plastic zones from extracted stress intensity factor ranges

The extraction of the effective stress intensity factor allowed for the direct estimation of the stress fields acting at the crack tip. Starting from these fields, it was possible to determine the shape and the dimension of cyclic plastic zones.[6] The stresses were computed as

$$
\begin{cases}
\sigma_x = \dfrac{K_I}{\sqrt{2\pi r}}(F_{Ix} + tF_{IIx}) \\[2mm]
\sigma_y = \dfrac{K_I}{\sqrt{2\pi r}}(F_{Iy} + tF_{IIy}) \\[2mm]
\tau_{xy} = \dfrac{K_I}{\sqrt{2\pi r}}(F_{Ixy} + tF_{IIxy})
\end{cases}
\tag{10}
$$

and the F terms in Eq. (10) were calculated as shown in Eqs (11) and (12), and where $t = K_{II}/K_I$.

$$
\begin{cases}
F_{Ix} = \mathrm{Re}\left[\dfrac{\mu_1\mu_2}{\mu_1 - \mu_2}\left(\dfrac{\mu_2}{\sqrt{\cos\vartheta + \mu_2\sin\vartheta}} - \dfrac{\mu_1}{\sqrt{\cos\vartheta + \mu_1\sin\vartheta}}\right)\right] \\[4mm]
F_{Iy} = \mathrm{Re}\left[\dfrac{1}{\mu_1 - \mu_2}\left(\dfrac{\mu_1}{\sqrt{\cos\vartheta + \mu_2\sin\vartheta}} - \dfrac{\mu_2}{\sqrt{\cos\vartheta + \mu_1\sin\vartheta}}\right)\right] \\[4mm]
F_{Ixy} = \mathrm{Re}\left[\dfrac{\mu_1\mu_2}{\mu_1 - \mu_2}\left(\dfrac{1}{\sqrt{\cos\vartheta + \mu_1\sin\vartheta}} - \dfrac{1}{\sqrt{\cos\vartheta + \mu_2\sin\vartheta}}\right)\right]
\end{cases}
\tag{11}
$$

$$
\begin{cases}
F_{IIx} = \mathrm{Re}\left[\dfrac{1}{\mu_1 - \mu_2}\left(\dfrac{\mu_2^{\,2}}{\sqrt{\cos\vartheta + \mu_2\sin\vartheta}} - \dfrac{\mu_1^{\,2}}{\sqrt{\cos\vartheta + \mu_1\sin\vartheta}}\right)\right] \\[4mm]
F_{IIy} = \mathrm{Re}\left[\dfrac{1}{\mu_1 - \mu_2}\left(\dfrac{1}{\sqrt{\cos\vartheta + \mu_2\sin\vartheta}} - \dfrac{1}{\sqrt{\cos\vartheta + \mu_1\sin\vartheta}}\right)\right] \\[4mm]
F_{IIxy} = \mathrm{Re}\left[\dfrac{1}{\mu_1 - \mu_2}\left(\dfrac{\mu_1}{\sqrt{\cos\vartheta + \mu_1\sin\vartheta}} - \dfrac{\mu_2}{\sqrt{\cos\vartheta + \mu_2\sin\vartheta}}\right)\right]
\end{cases}
\tag{12}
$$

Because the single crystal exhibits anisotropic behaviour, Hill's extension of the von Mises' yield criterion was used.[37] The yield criterion in quadratic form is expressed as proposed in Eq. (13).

$$E(\sigma_y - \sigma_z)^2 + G(\sigma_z - \sigma_x)^2 + H(\sigma_x - \sigma_y)^2 + 2L\tau_{xy}^2$$
$$+ 2M\tau_{xz}^2 + 2N\tau_{yz}^2 = 1 \qquad (13)$$

where E, G and H are coefficients that characterise the anisotropy in the normal directions, and L, M and N are the coefficients that characterise the shear anisotropy. These parameters can be calculated according to Eq. (14), where X, Y and Z are the yield stresses in the principal directions and S is the shear yield stress. Assuming plane stress because the specimens are thin, $\sigma_z = \tau_{xz} = \tau_{yz} = 0$, Eq. (13) reduces to Eq. (15).

$$\begin{cases} 2E = -\dfrac{1}{X^2} + \dfrac{1}{Y^2} + \dfrac{1}{Z^2} \\[2mm] 2G = \dfrac{1}{X^2} - \dfrac{1}{Y^2} + \dfrac{1}{Z^2} \\[2mm] 2H = \dfrac{1}{X^2} + \dfrac{1}{Y^2} - \dfrac{1}{Z^2} \\[2mm] 2N = \dfrac{1}{S^2} \end{cases} \qquad (14)$$

$$(G + H)\sigma_x^2 - 2H\sigma_x\sigma_y + (E + H)\sigma_y^2 + 2N\tau_{xy}^2 = 1 \quad (15)$$

To find the plastic zone, Eq. (10) is substitute into Eq. (15) SS and solved for the plastic zone radius, r_p. As suggested by Rice,[22] cyclic plastic zone radius, Δr_p is evaluated approximately as one quarter of the monotonic r_p, given in Eq. (16).

is under pure Mode I loading. In contrast to the round polycrystalline shape obtained considering isotropic behaviour, the anisotropic cyclic plastic zone for a pure Mode I loaded crack showed two marked lobes extending from the crack tip towards the crack flanks. At 50% of the maximum applied load, the cyclic plastic zone area is only 0.00307 mm^2, as shown in Fig. 9a. The maximum cyclic plastic zone is shown in Fig. 9b, and its area is 0.0332 mm^2. In this condition, strains around the crack tip are very concentrated and greater than 1%.

The presence of Mode II loading in the [111] case caused the cyclic plastic zone shape to be asymmetric. The cyclic plastic zone exhibits two different lobes: the upper one extends at an angle of 87° respect to the horizontal, whereas the lower one is at 77°. At 50% of the maximum applied load (Fig. 9c), the cyclic plastic zone extension was 0.0104 mm^2, whereas the maximum area registered was 0.2410 mm^2 (Fig. 9d). This is eight times bigger than the one measured in the [001] case. Even in this case, the strains measured around the crack tip were larger than 1%. The presence of sliding also influenced the strain field, which is asymmetric. A high strain zone started from the crack tip and covered the area in which the crack will propagate, together with a secondary strain area that stayed at 64° under the crack tip.

Cyclic plastic zones in single crystals can be described following several additional methods. In particular, a model based on double slip was employed to describe the effects of crystallographic orientations on the size and shape of the plastic zone.[31] In Haynes 230, a face-centred cubic material, it has been demonstrated that [111] oriented crystals can have up to six active slip systems and

$$\Delta r_p = \frac{1}{4} r_p = \frac{\Delta K^2_{I,eff}}{8\pi} \Big[(G + H)(F_{Ix} + tF_{IIx})^2 - 2H(F_{Ix} + tF_{IIx})(F_{Iy} + tF_{IIy}) + (E + H)(F_{Iy} + tF_{IIy})^2 + 2N(F_{Ixy} + tF_{IIxy})^2 \Big]$$
$$(16)$$

During measurement cycles, many images were acquired allowing for the observation of the evolution of stresses and strains around the crack tip. The cyclic plastic zone was evaluated according to Eq. (16), using the stress intensity factor ranges obtained from regression, while strains were evaluated using DIC. Strains were calculated from the partial derivatives of the displacement fields using the Lagrange strain tensor equations. In order to obtain smooth results, displacements were locally approximated with a first-order polynomial. The strains inside the plastic zones are shown in Fig. 9 for the loading portion of a fatigue cycle up to the maximum load for each specimen tested during this study.

The [001] crystal case, presented in Fig. 9a and b, showed a symmetric plastic zone, because the specimen

the number of active systems in a [001] orientation can be eight. Taking into account the presence of significant slip, the adoption of a continuum model, such as Hill's yield criterion, and its results should only be used as an initial estimation. In the following paragraph, the plastic zones obtained from finite element method (FEM) simulations considering single crystal plasticity are proposed and discussed.

Cyclic plastic zones from numerical simulations with single crystal plasticity

Inelastic deformation and crack propagation in single crystals are related to the irreversibility of slip. An accurate analysis of the area surrounding the crack tip should
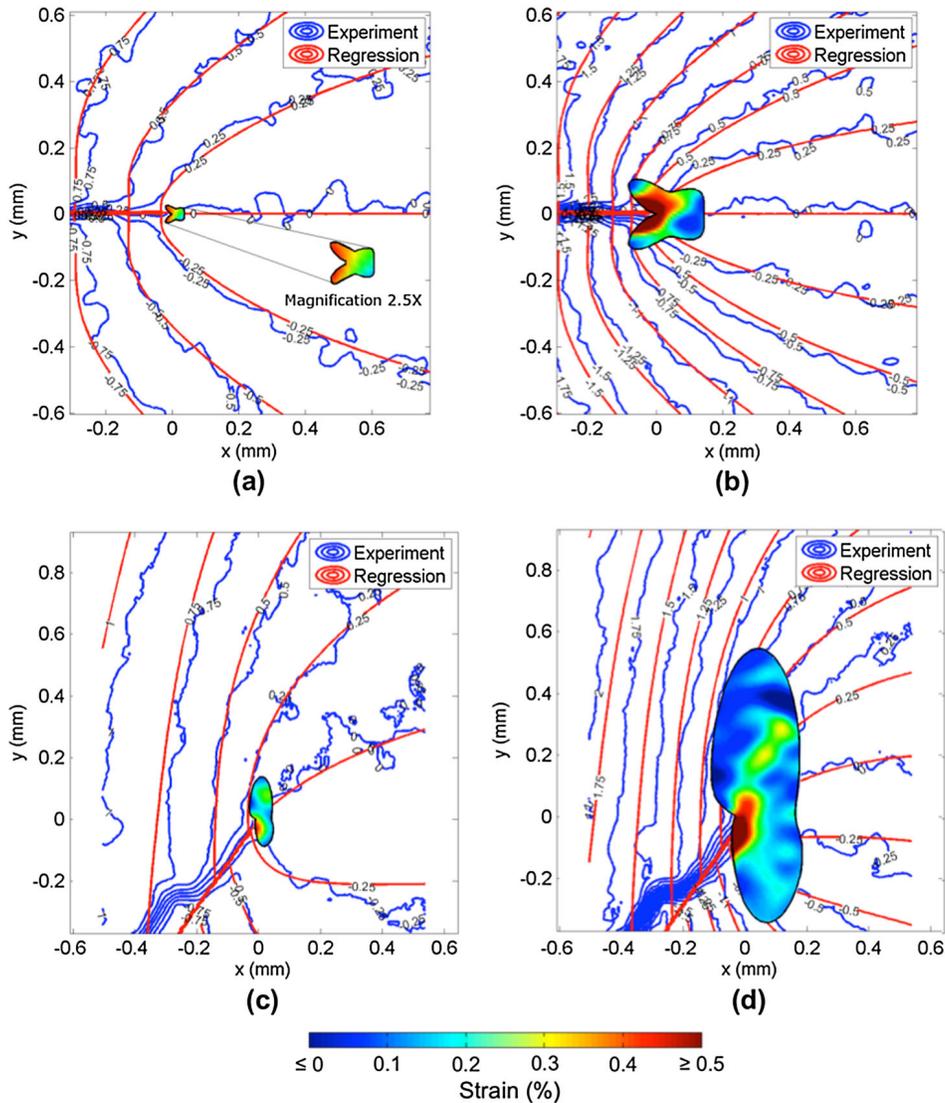
Fig. 9 Cyclic plastic zones calculated according to Hill's criterion and vertical contours in micrometres for the two considered orientations. (a) and (b) : [001] oriented specimen with a crack length of 0.95 mm with an applied load equal to 50% and 100% of the maximum load, respectively. The cyclic plastic zone area, $A_{\Delta rp}$, at the maximum load is equal to 0.03320 mm². (c) and (d): [111] oriented specimen with a crack length of 1.66 mm with an applied load equal to 50% and 100% of the maximum load, respectively. $A_{\Delta rp}$ at the maximum load is equal to 0.2410 mm².

take into account single crystal mechanical behaviour, and an approach based on continuum mechanics, like the one presented in the previous section, should be taken only as a preliminary result. In this section, a brief analysis of the crystal plasticity model adopted for plastic zone evaluation is given, together with the numerical results obtained for the two tested crystal orientations.

The kinematical theory of crystals is mainly due to the initial work of Taylor[38] and the mathematical formulations by Hill,[24] Rice,[27] Hill and Rice[25] and Asaro *et al.*[26] In this framework, the crystal deforms by two distinct mechanisms:

- plastic deformation, which consists of material shearing relative to a crystal lattice;
- elastic deformation of the lattice and material together.

In crystal plasticity theory, the deformation gradient F is not given by the sum of an elastic and a plastic part but is evaluated as the product of the deformation gradient associated to elastic loading, F^*, and of the deformation gradient that takes into account inelastic strains, F^p, adopting the multiplicative decomposition originally proposed by Lee[39]:

$$F = F^* \cdot F^P \qquad (17)$$

The main assumption of this model is that inelastic deformation is solely due to plastic shearing in crystallographic slip systems, as proposed in Eq. (18), where $s^{(a)}$ and $m^{(a)}$ are, respectively, the slip direction and the normal to slip plane of the α-th slip system, and $\dot{\gamma}^{(\alpha)}$ is the associated slip rate.

$$\dot{F}^{P}\cdot F^{P-1} = \sum_{\alpha}\dot{\gamma}^{(\alpha)}s^{(\alpha)}m^{(\alpha)} \qquad (18)$$

The crystalline slip is modelled to obey Schmid's law: the slipping rate $\dot{\gamma}$ in each α-th slip system is related to the external applied stress through the Schmid stress, τ, which is the resolved shear stress when the elastic deformations can be neglected, as

$$\dot{\gamma}^{(\alpha)} = a\left(\frac{\tau^{(\alpha)}}{g^{(\alpha)}}\right)^{z} \qquad (19)$$

where α is a constant, $g^{(\alpha)}$ is a variable describing the current strength of the α-th slip system and z is the rate sensitivity exponent.

The increment in the yield strength of each slip system follows what is proposed in Eq. (20), where $h_{\alpha\beta}$ is the hardening matrix.

$$\dot{g}^{(\alpha)} = \sum_{\beta}h_{\alpha\beta}\dot{\gamma}^{(\beta)} \qquad (20)$$

The diagonal terms of the hardening matrix are called self-hardening moduli, whereas the extra-diagonal terms are defined as latent hardening moduli. Pierce, Asaro and Needleman proposed a simple form for the self-hardening moduli[26]:

$$h_{\alpha\alpha} = h_0 \ \sec h^2\left|\frac{h_0\gamma}{\tau_s - \tau_0}\right| \qquad (21)$$

where there is no sum on α and h_0 is the initial hardening modulus, τ_0 is the yield stress that equals the initial value of the current strength $g^{(\alpha)}(0)$, τ_s is the stress where large plastic flow initiates, and γ is the Taylor cumulative shear strain on all slip systems:

$$\gamma = \sum_{\alpha}\int_{0}^{t}|\dot{\gamma}^{(\alpha)}|dt \qquad (22)$$

The latent hardening moduli are considered as a fraction of the self-hardening moduli, as expressed in Eq. (23).

$$h_{\alpha\beta} = qh_{\alpha\alpha} \qquad (a\neq\beta) \qquad (23)$$

In the case of this study, the value of the constant q is assumed to be equal to zero, so no interaction between the slip systems is considered. Single crystal plasticity behaviour is implemented in a commercially available software (Abaqus by Dassault Systèmes, Providence, Rhode Island, USA) in terms of a User Material (UMAT) external subroutine. A description of the subroutine is given by Huang.[40]

Numerical models implementing crystal plasticity were developed for the two tested crystal orientations. Simulations were performed on 2D models, and plane stress was assumed, because the specimens are thin. The crack length considered in these simulations was the same as those analysed in the previous section in order to make a comparison between the two. The employed plasticity model constants were obtained by fitting experimental tensile stress/strain curves obtained from unnotched Haynes 230 single crystals. Material constants are shown in Table 4.

Table 4 Coefficients employed for finite element method simulations

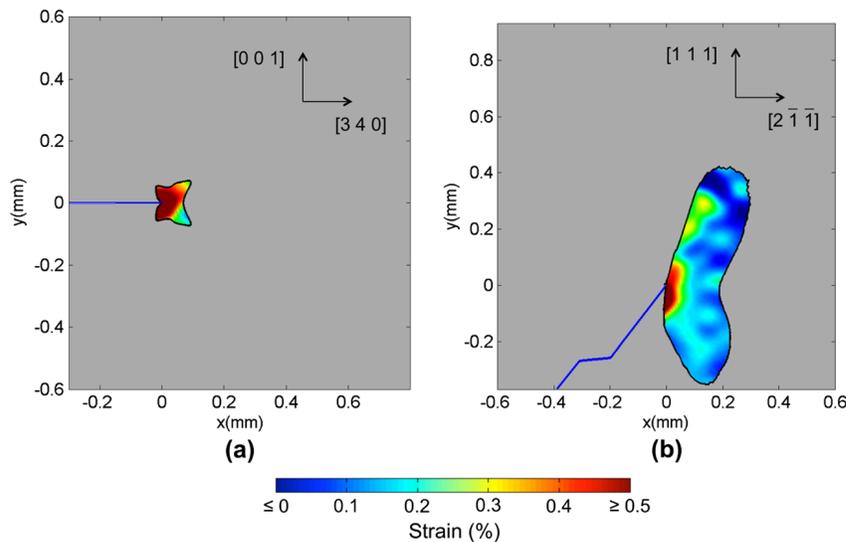| α	z	h_0	τ_s	τ_0
0.001	10	155	130	80

Fig. 10 Cyclic plastic zone calculated from single crystal plasticity simulation. (a) [001] specimen with a 0.96 mm long crack. Cyclic plastic zone extension, $A_{\Delta rp}$, is equal to 0.0116 mm². (b) [111] specimen with a 1.66 mm long crack. Cyclic plastic zone extension, $A_{\Delta rp}$, is equal to 0.1455 mm².

Because, in the considered plasticity model, there is no explicit yielding, the extension of the plastic zone was evaluated considering Hill's anisotropic yield criterion. Eq. (16) was employed during these calculations. The cyclic plastic zone was obtained considering $\Delta r_p = 1/4 r_p$, as suggested by Rice.[22]

In Fig. 10a, the results obtained for the [001] oriented crystal are presented. Respective to the cyclic plastic zone obtained from DIC displacements, the plastic zone presents a similar shape. In this case, the lobes extending towards the cracks flanks are smaller. As expected, the plastic zone shape is symmetric, because no Mode II was experienced during the test, and its size is smaller, 0.0116 mm^2 versus the 0.0307 mm^2 measured according to DIC. The vertical strains measured by DIC inside the cyclic plastic zone are in agreement with the numerical results, as strains are rapidly decreasing moving from the crack tip. The maximum shear stress measured at the crack tip is 324 MPa.

As observed in the previous section, the cyclic plastic zone obtained from numerical simulation for the [111] orientation is also asymmetric, as shown in Fig. 10b: following the same pattern, the main lobe of the plastic zone extends in the upper part of the specimen. The farthest point from the crack tip is at 62° from the horizontal. The angle calculated by FEM analysis is smaller than the one provided by Hill's criterion. The same observations can be made with the small lobe, which extends under the crack tip at 67°. The cyclic plastic zone calculated by FEM extends for 0.1455 mm^2 around the crack tip and, confirming what observed in the [001] case, is smaller than the one calculated from experimental displacements. The cyclic plastic zones obtained from FEM for the two different orientations have a different extension, confirming the observations obtained analysing the experimentally measured zones. The maximum shear stress is calculated at the tip and is 357 MPa.

CONCLUSIONS

In this study, fatigue crack growth at room temperature in Haynes 230 single crystals was analysed. In particular, several different techniques were employed:

1 Stress intensity factor ranges (Modes I and II) were calculated with a least-squares regression technique, starting from the displacements measured by DIC. Results were compared with those obtained from polycrystalline experiments, displaying a similar behaviour.
2 Crack tip opening/sliding displacements were measured by observing the relative displacements of the crack flanks with two-point virtual extensometers. Both the cracks opened at 20% of the maximum applied load. During mixed-mode propagation, Mode II sliding was observed before Mode I opening.

3 Anisotropic Hill's yield criterion was adopted to obtain an initial estimate of the cyclic plastic zone around the crack tip. Results were compared with the strains measured by DIC. The cyclic plastic zone calculated for the [001] specimen was eight times smaller than the one observed for the [111] orientation.
4 Numerical simulations were carried out to calculate the plastic zone around the crack tip, considering single crystal plasticity. The results showed good agreement with the measured strains for the same effective K-loads. Consistent with the experimental results, the cyclic plastic zone around the crack tip of the [111] was greater than the one observed in the [001] case, underlining the importance of ΔK_{II} in cyclic plastic zone shape and size.

REFERENCES

1 Reed, R. C. (2006) The Superalloys: Fundamentals and Applications. Cambridge University Press, Cambridge, UK.
2 Paris, P. C., Erdogan, F. (1963) A critical analysis of crack propagation laws. *J. Basic Eng.*, **85**, 528–533.
3 Duquette, D., Gell, M. (1972) The effects of environment on the elevated temperature fatigue behavior of nickel-base superalloy single crystals. *Metall. Mater. Trans. B.*, **3**, 1899–1905.
4 Tanaka, K. (1974) Fatigue crack propagation from a crack inclined to the cyclic tensile axis. *Eng. Fract. Mech.*, **6**, 493–498.
5 Williams, M. L. (1957) On stress distribution at base of stationary crack. *Am. Soc. Mech. Eng. - Trans. - J. Appl. Mech.*, **24**, 109–114.
6 Sih, G. C., Paris, P. C., Irwin, G. R. (1965) On cracks in rectilinearly anisotropic bodies. *Int. J. Fract. Mech.*, **1**, 189–203.
7 Riddell, W. T., Piascik, R. S., Sutton, M. A., Zhao, W., McNeill, S. R., Helm, J. D. (1999) Determining fatigue crack opening loads from near-crack-tip displacement measurements. *ASTM STP - 1343*. 157.
8 Sutton, M. A., Zhao, W., McNeill, S. R., Helm, J. D., Piascik, R. S., Riddell, W. T. (1999) Local crack closure measurements: development of a measurement system using computer vision and a far-field microscope. *ASTM STP - 1343*. 145.
9 Elber, W. (1970) Fatigue crack closure under cyclic tension. *Eng. Fract. Mech.*, **2**, 37–45.
10 Elber, W. (1971) The significance of fatigue crack closure. *Damage Tolerance in Aircraft Structures: A Symposium Presented at the Seventy-third Annual Meeting American Society for Testing and Materials, Toronto, Ontario, Canada, 21–26 June 1970.* ASTM International, 230.
11 McNeill, S. R., Peters, W. H., Sutton, M. A. (1987) Estimation of stress intensity factor by digital image correlation. *Eng. Fract. Mech.*, **28**, 101–112.

12 Carroll, J., Efstathiou, C., Lambros, J., Sehitoglu, H., Hauber, B., Spottswood, S., Chona, R. (2009) Investigation of fatigue crack closure using multiscale image correlation experiments. *Eng. Fract. Mech.*, **76**: 2384–2398.

13 Yoneyama, S., Morimoto, Y., Takashi, M. (2006) Automatic evaluation of mixed-mode stress intensity factors utilizing digital image correlation. *Strain.*, **42**, 21–29.

14 Pataky, G. J., Sangid, M. D., Sehitoglu, H., Hamilton, R. F., Maier, H. J., Sofronis, P. (2012) Full field measurements of anisotropic stress intensity factor ranges in fatigue. *Eng. Fract. Mech.*, **94**, 13–28.

15 Pataky, G. J., Sehitoglu, H., Maier, H. J. (2013) High temperature fatigue crack growth of Haynes 230. *Mater Charact*, **75**, 69–78.

16 Lankford, J., Davidson, D. L., Chan, K. S. (1984) Influence of crack tip plasticity in the growth of small fatigue cracks. *Metall. trans. A, Phys. metall. mater. sci.*, **15 A**, 1579–1588.

17 Nowack, H., Trautmann, K. H., Schulte, K., Luetjering, G. (1979) Sequence effects on fatigue crack propagation; mechanical and microstructural contributions. *ASTM Special Technical Publication*. 36.

18 Xin, G., Hangong, W., Xingwu, K., Liangzhou, J. (2010) Analytic solutions to crack tip plastic zone under various loading conditions. *Eur. J. Mech., A/Solids*, **29**, 738–745.

19 Zhang, J. P., Venugopalan, D. (1987) Effects of notch radius and anisotropy on the crack tip plastic zone. *Eng. Fract. Mech.*, **26**, 913–925.

20 Gao, H., Alagok, N., Brown, M. W., Miller, K. J. (1985) Growth of fatigue cracks under combined Mode I and Mode II loads. *ASTM STP - 853*. 184.

21 Betegon, C., Hancock, J. W. (1991) Two-parameter characterization of elastic-plastic crack-tip fields. *Trans. ASME J. Appl. Mech.*, **58**, 104–110.

22 Ricel, J. R. (1966) Mechanics of crack tip deformation and extension by fatigue.

23 McClung, R. C., Sehitoglu, H. (1989) On the finite element analysis of fatigue crack closure—2. Numerical results. *Eng. Fract. Mech.*, **33**, 253–272.

24 Hill, R. (1966) Generalized constitutive relations for incremental deformation of metal crystals by multislip. *J. Mech. Phys. Solids.*, **14**, 95–102.

25 Hill, R., Rice, J. R. (1972) Constitutive analysis of elastic-plastic crystals at arbitrary strain. *J. Mech. Phys. Solids.*, **20**, 401–413.

26 Needleman, A., Asaro, R. J., Lemonds, J., Peirce, D. (1985) Finite element analysis of crystalline solids. *Comput. Meth. Appl. Mech. Eng.*, **52**, 689–708.

27 Rice, J. R. (1971) Inelastic constitutive relations for solids: an internal-variable theory and its application to metal plasticity. *J. Mech. Phys. Solids.*, **19**, 433–455.

28 Rice, J. R., Hawk, D. E., Asaro, R. J. (1990) Crack tip fields in ductile crystals. Non-linear Fracture. Springer, The Netherlands, pp. 301–321.

29 Flouriot, S., Forest, S., Cailletaud, G., Köster, A., Rémy, L., Burgardt, B., Gros, V., Mosset, S., Delautre, J. (2003) Strain localization at the crack tip in single crystal CT specimens under monotonous loading: 3D finite element analyses and application to nickel-base superalloys. *Int. J. Fract.*, **124**, 43–77.

30 Potirniche, G. P., Daniewicz, S. R. (2003) Analysis of crack tip plasticity for microstructurally small cracks using crystal plasticity theory. *Eng. Fract. Mech.*, **70**, 1623–1643.

31 Gall, K., Sehitoglu, H., Kadioglu, Y. (1996) Plastic zones and fatigue-crack closure under plane-strain double slip. *Metall. Mater. Trans. A Phys. Metall. Mater. Sci.*, **27 A**, 3491–3502.

32 Potirniche, G. P., Daniewicz, S. R., Newman, J. C. (2004) Simulating small crack growth behaviour using crystal plasticity theory and finite element analysis. *Fatigue fract. Eng. Mater. Struct.*, **27**, 59–71.

33 Shah, P. D., Tan, C. L., Wang, X. (2006) T-stress solutions for two-dimensional crack problems in anisotropic elasticity using the boundary element method. *Fatigue fract. Eng. Mater. Struct.*, **29**, 343–356.

34 Hertzberg, R. W. (1996) Deformation and Fracture Mechanics of Engineering Materials. Wiley New York, New York.

35 Chen, Q., Kawagoishi, N., Nisitani, H. (2000) Evaluation of fatigue crack growth rate and life prediction of Inconel 718 at room and elevated temperatures. *Mater. Sci. Eng. A*, **277**, 250–257.

36 Lu, Y. L., Liaw, P. K., Wang, G. Y., Benson, M. L., Thompson, S. A., Blust, J. W., Browning, P. F., Bhattacharya, A. K., Aurrecoechea, J. M., Klarstrom, D. L. (2005) Fracture modes of HAYNES alloy during fatigue-crack-growth at room and elevated temperatures. *Mater. Sci. Eng. A*, **397**, 122–131.

37 Hill, R. (1950) Mathematical theory of plasticity. Oxford, UK, Oxford University Press pp. 318–325.

38 Taylor, G. I. (1938) Plastic strain in metals. *J. Inst. Metals.*, **62**, 307–324.

39 Lee, E. H. (1969) Elastic-plastic deformation at finite strains. *J. Appl. Mech.*, **36**, 1–6.

40 Huang Y. (1991) A user-material subroutine incorporating single crystal plasticity in the ABAQUS finite element program. Harvard Univ.